Enhancement of a Diesel Engine Inlet Port for Pollutant Reduction and Performance Optimization

S. E. Razavi
Professor Assistant
School of Mechanical
Tabriz University
Razavi@tabrizu.ac.ir

S. M. Lashkarpour*
PhD Student
Motorsazan R&D Department
Lashkarpour@gmail.com

S. Marami
PhD Student
Olum Tahghighat University of Tehran
Samira.Marami@gmail.com

Corresponding Author*
Received: Dec. 18,2010
Accepted in revised form: Feb. 14,2011

Abstract

This research uses computational modeling to explore another method to increase diesel engine performance while maintaining low pollutant emission levels. Previous studies have shown that injection-rate profiles and injector configurations play important roles on the performance and emissions of particulate and NOx in DI diesel engines. Since the most important engine design parameters, including filling efficiency, flame stability, performance and pollutant formation depend on the local flow field in inlet port and then in cylinder, the ability to accurately predict these more details is a key requirement for successful application of computational fluid dynamics techniques to design and optimization engines. In this work which is done at Motorsazan.Co in order to optimize inlet port shape, a procedure is outlined for producing a computational mesh for intake port and in-cylinder geometry on 135TI diesel engine at various intake port shapes. After modeling the combustion chamber with inlet port, AVL FIRE software has been employed for grid generation and numerical simulation in an open cycle mode. The numerical results are validated by corresponding experimental data for base line engine. Concerning the design limitations, two new helical ports are introduced and simulated using the same solver, boundary and initial conditions. Final performance and pollutant emission results, obtained from new models are compared with those of the base model and the model with the best results is introduced as the optimum among all. This work demonstrates that multidimensional modeling at an open cycle can now be used to gain insight into the combustion process and provide direction to explore new engine concepts.

Keywords: *Diesel Engine, Inlet Port, Helical Port, AVL FIRE.*

1- Introduction

Experience and simulation shows that the fluid pattern in the combustion chamber has great influence on spray atomization and ignition delay. Thus, to reach a superior design, investigation of this phenomenon is essential.

One of the results of increasing mixing rate in turbulent flow is to raise the probability of soot particle in contact with oxidizer in the combustion chamber. This is possible by conducting inlet port air flow in order to produce swirl in the combustion chamber. There are several ways of enhancing turbulent mixing process, such as increasing the injection pressure, multi stage injection and inlet port improvement. Enhancing air and fuel mixing which is a result of increasing inlet air turbulence could lead to soot reduction. In part load condition, increasing swirl will lead to reduction in soot and HC pollutant where it also decreases fuel consumption due to better air fuel mixing [1]. The NOx pollutant slightly increases by growing the inlet air swirl. At higher loads, increasing air swirl has smaller effect on soot and fuel consumption reduction, however higher temperature can lead to elevation of NOx emission [2]. In contrast, reducing volumetric efficiency and increasing heat transfer between the fluid and wall through the induction stroke could reduce NOx pollutant [3].

There are two general ways for producing swirl through induction stroke. The first way is to conduct parallel flow leaving from inlet port towards the cylinder wall. This flow spins down through the cylinder axis and produces desired swirl. The second way is produced through the inlet port. In this method, the air flow is forced to swirl around the inlet valve axis through cylinder inlet flow which has gained angular momentum.

Effects of the air flow pattern produced by two inlet port in steady and transient mode, along with the transient mode effects (and valve timing) on the swirl intensity in combustion chamber is studied by Rutland et al [4]. Simulation of flow in the helical port with the in cylinder flow characteristics using KIVA3V is also investigated by Jong Gyu Kim et al. [5], and they proved that the angular momentum is generated in the inlet port before the cylinder. Furthermore, a reverse flow is generated as this swirling flow makes contact with cylinder wall where it strikes the main swirl flow. This results in creation of a unit swirling flow at the end of induction stroke. Kawashima and Ogawa [6] used two separate ports (tangential and helical) to change swirl ratio in the cylinder (helical port for generating high swirl and tangential for low swirl). Then, by analyzing the helical port separately they showed that the main factor in generating high swirl ratio is directing the flow through inlet valve sit efficiently. After that, they studied the effect of several combinations of helical and tangential ports and analyzed the swirl ratio with the flow factor in each case. The objective of the present study was to investigate the effects of intake port geometry on the performance and emission which is one of the design parameters that has to be optimized in the engine. Regarding the effects of induced swirl by inlet port, some works have been done to analyze the exiting flow from the inlet port and its effects on the flow characteristics. It should be noted that open cycle numerical studies has not got a long history.

Methodology

This study is done on Motorsazan 135TI four cylinder direct injection diesel engines. The engine under study is a commercial DI, water cooled four cylinders, in-line, turbocharged aspirated diesel engine with DPA (Distributive pump Type A) injection pump, whose major specifications are shown in table 1.

Table 1. 135TI engine specifications.

Number of Intake valves	1 per cylinder
Bore × Stroke (mm)	100 × 127
Compression ratio	17.5:1
Engine Speed (rpm)	2000
Aspiration	Turbo charged
Fuel Injection	DPA Pump
Start of Injection (deg btdc)	4
Duration of Injection (deg)	20
Number of Nozzle orifice × diameter (mm)	5 × 0.276
IVC to EVO (deg atdc)	-146 to 95
Displacement (lit)	3.99
Rate of fuel injected (kg/h)	15.22
Combustion chamber	Reentrant

Figure1 shows Schematic diagram of experimental setup. As shown in this figure, the mass flow meter operates on a hot wire anemometer principle. It is possible to cover a very large measuring range with constant accuracy (max. error 1% of the measured value). With a high accuracy mass flow sensor, the fuel consumption is determined continuously via direct mass flow measurement in kg/h (Fuel meter sys. In fig.1). Temperatures of cooling water,

lubricating oil, inlet air and exhaust gases were also measured to ensure proper engine operating conditions. A data acquisition system was used to collect the important data and store them in a personal computer in order to analyze them precisely (By A/D Convertor). A piezoelectric type pressure transducer (Indi Modul 621) was flush-mounted on the combustion chamber for routine sampling of the cylinder pressure at every 0.1 crank angle. Engine crank shaft position was determined by a crank angle encoder. The fuel injector was instrumented by a hall-effect needle lift sensor which provided indications of the start and end of fuel injection events. Concentrations of particulates were determined by measuring filter weight before and after sampling (AVL SPC 472_Model CE 97). A separate probe was used for particulate matter (PM) sampling. The temperature of the probe was maintained above 190°C to prevent condensation. The exhaust sample was then diluted into a mini-dilution tunnel, using filtered dried air. The total mass flow rate of the tunnel (Gtot) and the hence mass flow rate of diluted air (Gdil) were measured and controlled by SPC. The mass flow rate of the exhaust flow was calculated as the difference of the other two flows. The heated probe was mounted after the mixing tank to sample the gaseous emissions in the exhaust. Other engine emissions were measured by using an AVL Dicom4000-class1 exhaust gas analyzer (Gas Analyzer). Unburned hydrocarbons, CO and CO_2 were measured by using a non-dispersive infrared detector while an electrochemical detector was used for O_2 and NOx measurements. Also air flow was measured by hot wire flow air meter.

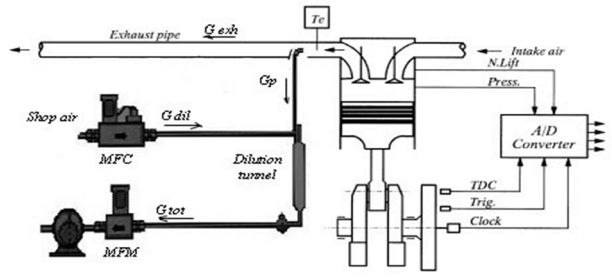

Fig 1. Schematic diagram of experimental set-up

Experiments were conducted on a DI diesel engine connected with a D.C. magnetic dynamometer. Pollutant emission and performance measurements were performed according to the (ECE-R96), at first mode of 8 mode procedure (full load power, speed -2000 rpm). To ensure the measurement accuracy, all emission analyzers were calibrated before each test run.

The emission measurements at each mode were repeated five times. The averaged values of repeated measurements were used in the analysis. From the repeated data points, the repeatability of the engine experiments can be estimated. The standard deviations over the means of the emission data are 0.85 for NOx, 4.2 for PM and 0.3 for fuel consumption. It could be found that NOx emission measurement repeatability was excellent, whereas all other measurements have decent repeatability.

Combustion pressure and emissions were monitored for base engine at full load condition. Inlet surface of the two designed helical port are quadrate. Due to design constraints (location and water canals positions) these inlet profiles are inevitable. Differences between the helical ports and the base are shown in Fig 2.

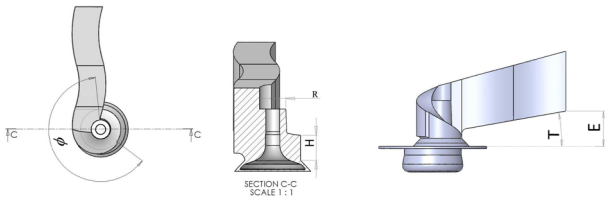

Models	ϕ	R(cm)	H(cm)	T°	E(cm)	$A(cm^2)$	Inlet Area Increase	$V(cm^3)$
Base Model	-	-	-	-	-	12.5	-	128.7
Model 1	227.8	13.2	34.9	10	32.6	14.3	12.2	198.4
Model 2	360.0	4.2	17.1	10	32.7	14.3	12.2	182.6

Fig 2. Design parameter list for the base and helical ports.

A cross section of the base model is shown in Figure 3.

Primary surface grid is generated by ICEM software with STL format and shown in Figure 4. The maximum grid size is 2 mm and it is generated to completely cover the desired surfaces.

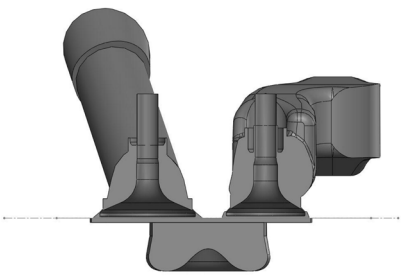

Fig 3. A cross section of the base port, CAD model in TDC.

.

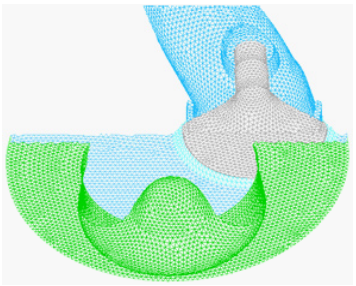

Fig 4. Cross section of the generated surface mesh in ICEM.

The final grid of the base engine and designed models are demonstrated in Figure 5.

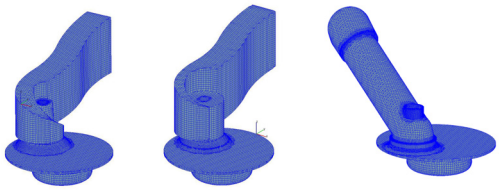

Fig 5. Final mesh, Base model (right), model no.1 (middle) and model no.2 (left).

Calculation starts from IVO = 340 °CA lasts till EVO = 815 °CA. To show the grid independency, in cylinder pressure curve vs. crank angle was used. The base grid was generated with three different meshes, 164245, 182526 and 231596 cells. The 164245 cells (at TDC) were selected as the final choice.

During induction, compression and expansion strokes, the generated mesh is divided into two sections. In the first section, air flow enters the combustion chamber through the inlet port from 340 °CA to 574 °CA. the Second section operates between 574 °CA and 815 °CA. In this section, inlet valve is closed so the inlet port and inlet valve are not included in overall system. To reduce the calculations in the second section, the port and valve grids were neglected from the calculations. Therefore, overall system was assumed as a closed cycle.

The SIMPLE algorithm is used as a domain solver. the Second order upwind scheme is used to solve continuity and turbulence equations. SMART scheme is also used to solve momentum and energy equations. The models are shown in Table 2.

Table 2. Models used in the simulation.

Turbulence model	RNG k-ε
Ignition model	SHELL (Halsted)
Combustion model	Magnussen time scale parameter
Soot oxidation model	Nagle and Strickland-Constable
Nitrogen oxides model	Extended Zeldovich (Heywood)
Spray dynamics	Wave model (Reitz)

Initial and boundary conditions which are used in the simulation (for base model) are based on the measurements done, using sensors installed on the engine and the engine working condition. Initial and boundary conditions are shown in Figure 6.

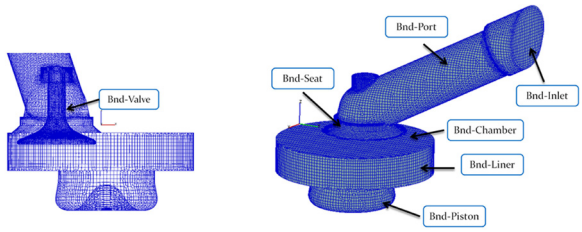

Boundary Conditions	Type of B.C
Bnd-Inlet	Inlet- From Sencor Data-T=400K
Bnd-Port	Wall – T=400K
Bnd – Seat	Wall – T=400K
Bnd - Valve	Wall – Mesh Movement- T=400K
Bnd - Chamber	Wall – T=500K
Bnd - Liner	Wall – T=450K
Bnd - Piston	Wall – Mesh Movement – T=450K
Initial Conditions	**Values**
Engine Speed	2000 rpm
T.K.E	8 m^2/s^2
T.L.S	0.01 m
Initial Chamber Pressure	126 Kpa
Initial Chamber Temperature	430K
Initial Port Pressure	120 Kpa
Initial Port Temperature	370K

Fig 6. boundary and initial conditions.

The calculations have been done in full load condition in 2000 rpm engine speed. Inlet air temperature is 130 C°. Figure 7 shows the inlet relative pressure at inlet port from 340 °CA to 815 °CA which is considered as inlet pressure boundary condition.

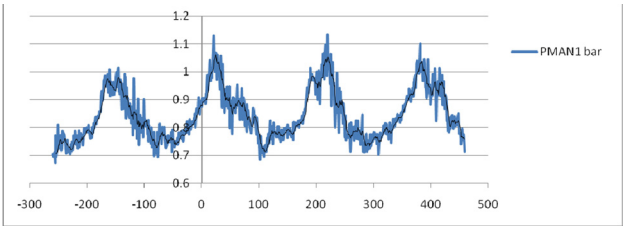

Fig 7. Inlet Manifold relative pressure vs. crank angle.

The injected fuel in each cycle was calculated based on Bsfc (Brake Specific fuel consumption). Initial condi-

tions for injection initiation with the injection duration are concluded (Figure 8). The relationship between injection pressure and injector needle lift is shown in Figure 8. As shown in Figure 8, when the pressure reaches 200 bars in 4 degree BTDC, the needle goings to open, this opening lasts 20 °CA. So the consumed fuel (about 6.5×10E-5 kg/cycle) is injected during 20 °CA. Numerical results of pollutants and measured engine performance values will be compared in the results and Discussion section.

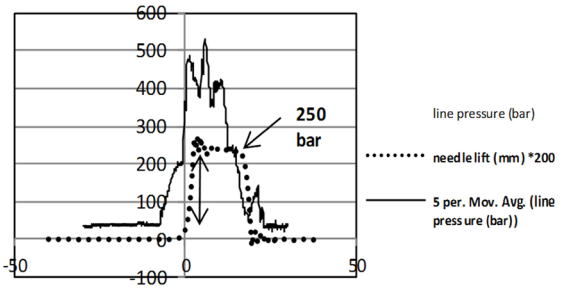

Fig 8. Injection pressure curve and injector needle lift with respect to crank angle.

Results and Discussion

Numerical and experimental results of in- cylinder pressure are compared in Figure 9. In- cylinder pressure curve accompanying the pollutant emissions will be used to validate the numerical results of simulated combustion chamber with the base inlet port. The pressure curve has an inflection at 720 °CA and the maximum pressure occurs at 732 °CA. This trend can be expected in all diesel engines. However, the maximum pressure does not go far from the point of inflection due to the fact that the start of injection is very close to TDC (Top Dead Center). The experimental data oscillation exists because of 1 °CA gap between data reading in pressure-crank angle facility, Pizo sensor accuracy and in cylinder oscillations. As seen in Figure 9, the graph of numerical results agrees with the experimental data of base engine (base model).

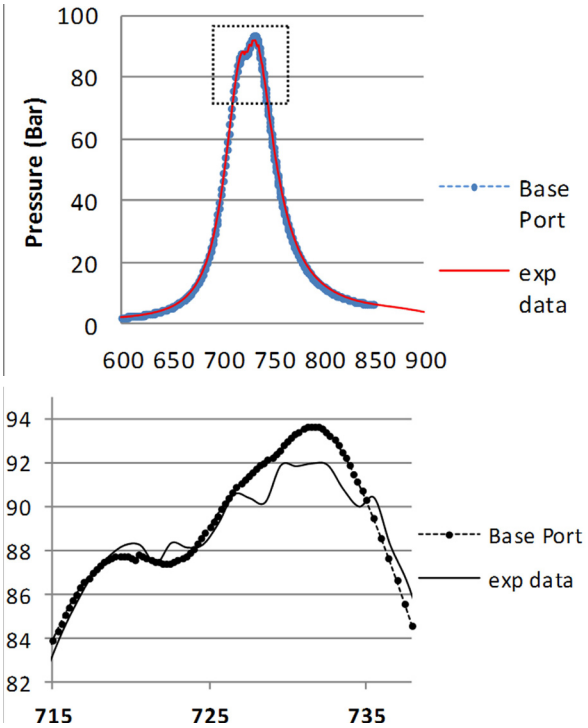

Fig 9. Pressure vs. crank angle curve of the base model for validation.

The pollutants values are in mass base which could be converted to g/kW.h by using in- cylinder mass. The engine power and speed is compared to the measured data. While pressure in Tabriz is lower than standard, all the experimental tests have been performed at the sea level condition. The simulated values of NOx and soot are compared with the experimental data in Figure 10.

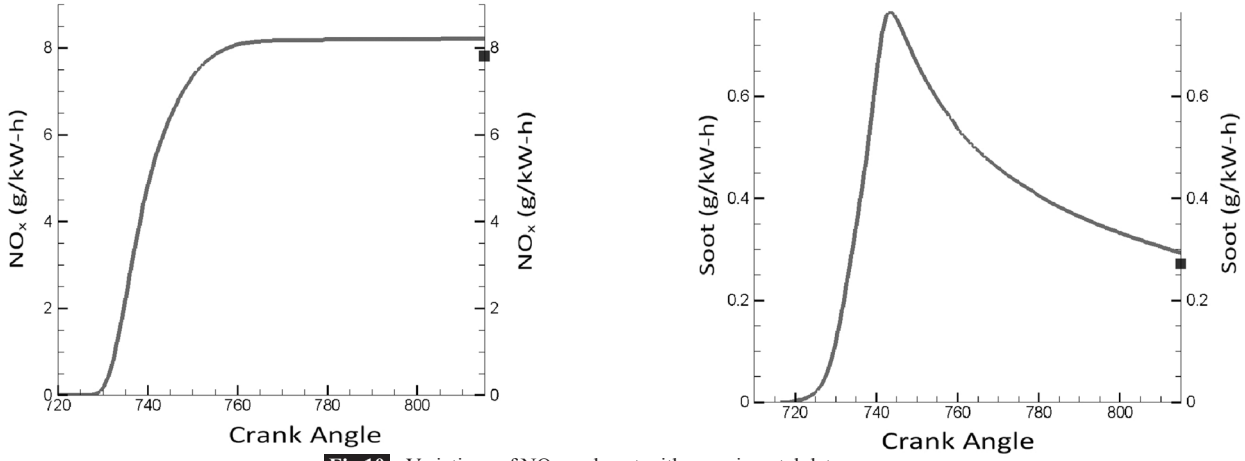

Fig 10. Variations of NOx and soot with experimental data.

Experimental and simulated results of engine power and pollutants are shown in table 3.

Table 3. Comparison between experimental and numerical results for base state.

Soot g/ kW.h	NOx g/ kW.h	Bsfc g/ kW.h	Break power kW	Indicated power kW	
0.271	7.81	259.22	61.62	83.21	Exp. data
0.292	8.23	248.48	60.63	81.33	Numerical results
7.5	5.1	4.14	1.28	2.19	Error (%)

Reasons of the variations on graphs demonstrated above are discussed later in this paper. Flow lines of the base model are shown in the Figure 11.

Fig 11. Flow vectors for base model.tion.

The streamlines are shown at 90 ° ATDC in Figure 11. One can conclude that the inlet flow from the port swerves as it contacts with the cylinder wall, then it swirls around the cylinder axis. Swirling flow through inlet port does not occur in the tangential ports and the flow enters combustion chamber, tangent to the valve seat.

The impact of exiting air jet on cylinder wall affects the air temperature in the combustion chamber. For justifying the air temperature in SOI[1], velocity vectors at different crank angles will be used. Velocity vectors and their orientation at 90° ATDC is shown in Figure 12.

1- Start Of Injection

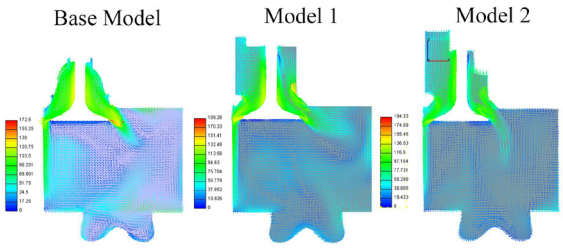

Fig 12. Velocity vectors at 90° ATDC for base port (left), port 1 (middle) and port 2 (right).

As shown in Figure 12, flow vectors of model 1 and model 2 have different orientations. Due to flow inlet, air swirl invigorates during the induction stroke. Swirling motion amplifies. as a result of angular momentum conservation. This increase is seen in all three models. However, this enhancement is greater in model 2, so model 2 will have higher swirl in SOI. The swirling flow in base model is generated by the contact of inlet flow to the wall and its orientation towards cylinder wall. In other models, swirling flow is the result of angular momentum in the port exit flow. Regarding Figure 13, the entering flow to combustion chamber is such that the striking action to the wall is less than other two models. This leads to reduction of heat transfer from chamber to the flow.

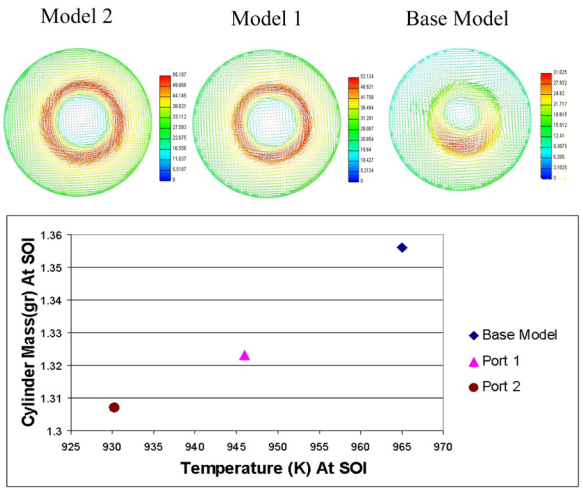

Fig 13. SOI temperature vs. chamber mass.

Thus, inlet flow in model 2 will receive lower heat during the induction stroke. During this stroke, flow impinging the wall leads to heat transfer to the fluid. However, during compression stroke, heat transfer created by impinging flow decreases and moving flow gets more important role.

During the induction stroke, because of the collision of the air flow with the wall and flow having a higher temperature than the cylinder wall (because of combustion in the previous cycles), the heat flux direction will be changed. It will be from the wall to the flow.

During the compression stroke, flow temperature is increasing till 630° ATDC where the heat fluxes direction changes and becomes reversed. At this stage, the swirling motion is very important for heat transfer to the wall. Increasing swirl enhances convection heat transfer. Regarding the higher swirl at SOI, temperature in port 2 is the lowest. This trend is shown in the Figure 13. Mixing characteristics during compression stroke will determine the quality and rate of air and fuel mixing process.

Considering the fact that turbulent viscosity indicates local mixing, it is a suitable parameter to examine. Turbulent viscosity is a function of turbulent kinetic energy and turbulent dissipation.

As the fluid flow leaves the inlet valve and enters the chamber, it generates shearing layers which can produce velocity gradient and leads to turbulent kinetic energy generation. Turbulent kinetic energy reaches its maximum value at 70 ATDC which corresponds to the maximum piston velocity. Thus turbulent kinetic energy depends on the piston velocity. The turbulent kinetic energy for all three models is shown in Figure 14.

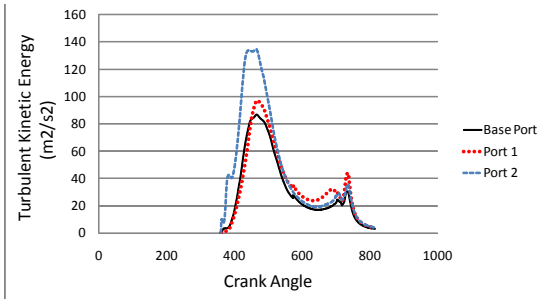

Fig 14. Turbulent kinetic energy for base model and 2 suggested models.

During compression stroke the majority of turbulent kinetic energy will be lost. Regarding Figure 14, one can conclude that in all three models, maximum turbulent kinetic energy occurs at the maximum piston velocity. Due to the highest inlet velocity in port 2, turbulent energy during induction stroke is higher than the other two models. As discussed turbulent kinetic energy is generated by the shearing layers and velocity gradient. As shown in Figure 12, there is also a vertical swirl in port 2 which disappears during compression stroke and leads to increased turbulent kinetic energy. However, according to Figure 14, at SOI and combustion early stages turbulent kinetic energy in port 1 has lower value. As shown in upper part of Figure 14, velocity contour has got more homogeneous profile than the base engine. This will lead into reduction in turbulent kinetic energy such that its value gets close to the value which base port has in SOI. However mean velocity in port 1 is higher than the base engine.

As shown in the Figure 15, in spite of using helical ports and the probability of reduction in mass flow rate and final mass, there are negligible differences in maximum mass flow rate for the three models.

Comparing accumulated mass at IVC one may conclude that volumetric efficiencies are almost equal in all three models. This is due to the large cross-sectional area and designing parameters.

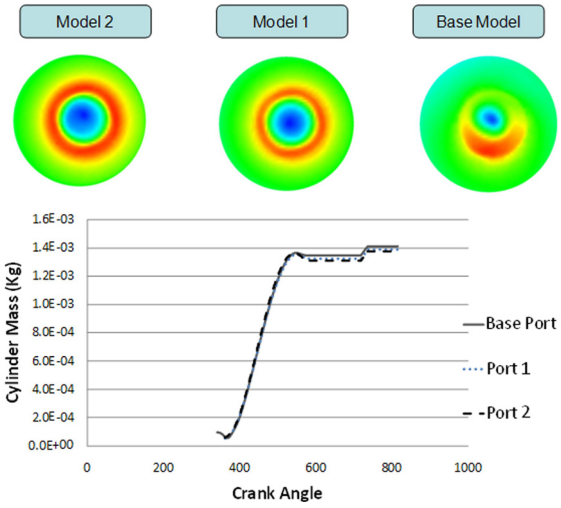

Fig 15. Comparison of inlet mass from EVC to ECO

Quantitative comparison of these values is shown in Table 4.

Table 4. Comparison of experimental and numerical results for volumetric efficiency.

	Air mass in IVC	Volumetric Efficiency٪	Error (%)
Experimental results	0.001454	94.42	-
Base model	0.001369	93.53	9.4
Model 1	0.001332	92.34	-
Model 2	0.001302	91.84	-

In cylinder pressure diagram for models are shown in Figure 16.

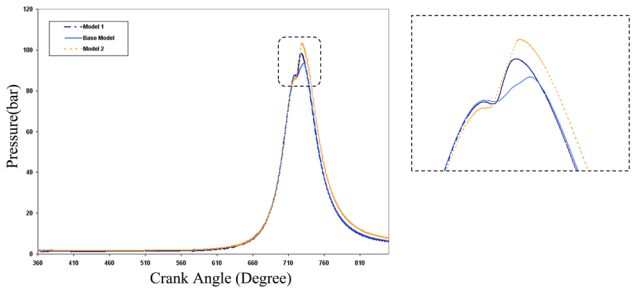

Fig 16. Comparing the in cylinder pressure for three models.

Details of pressure changes, power, and fuel consumption are shown in Table5.

Table 5. Comparison of pressure, power, and bsfc.

Model	Max. pressure (bar)	Max. pressure degree	Indicated power (HP)	bsfc g/kW.h	Bsfc red. (%)
Base model	93.6	731.5	83	248.4	-
Model 1	98.2	727.75	84.4	239.5	3.60
Model 2	103.1	728.75	86.3	234.2	4.12

As seen the pressure value in the primary maximum pressure value for all three models is close to each other (primary maximum in port 2 has lower value than others which is because of minor reduction in volumetric efficiency and relative temperature as discussed in Figure 16). The increasing trend of pressure curve is the same and there is no noticeable difference during induction and compression strokes. Regarding the analysis done in flow structure section (Figure 12), it is detected that in addition to temperature reduction in SOI, relative velocity is increased in model2 with respect to others. The velocity is swirling type and it has a neat trend (Figure 13). More temperature reduction in model 2 than two other model in addition to increasing relative velocity and also small difference between its turbulent kinetic energy rather than model 1 leads to minor differences between ignition delays in model2 with respect to the base model (Figure 17).

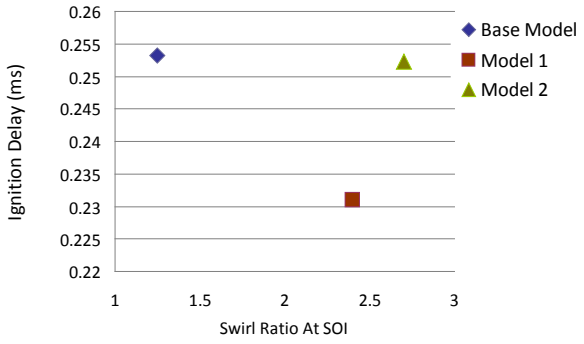

Fig 17. relation between ignition delay vs. swirl ratio at SOI.

According to Fuchs and Rutland [7], increasing swirl ratio should lead to reduction in ignition delay due to enhancement on fuel air mixing. However, as seen in Figure 17, this routine has been vanished in model 2. This is due to the effect of turbulent viscosity and temperature parameters at SOI. It is discussed that due to reduction in collision of air jet leaving inlet port to the cylinder wall during the induction stroke and increasing heat transfer to the wall during compression stroke, air temperature in model 2 has been reduced comparing to the base model which directly affected the ignition delay. Minor changes in turbulent kinetic energy relative to base model also intensify the temperature reduction. All these factors together led on little ignition delay difference between model 2 and base model. The relation between the ignition delay and the temperature at SOI is shown in Figure 18.

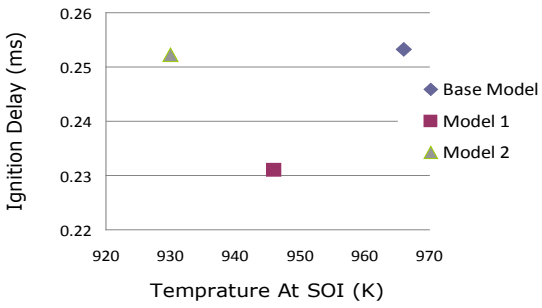

Fig 18. The relation of ignition delay and temperature at SOI.

The remarkable point in this section is smaller ignition delay compared to other engines studied in the papers which is because of higher cylinder pressure in later stages of compression stroke and higher temperature at cylinder in this moment. Heat release diagram for all three models are shown in Figure 19.

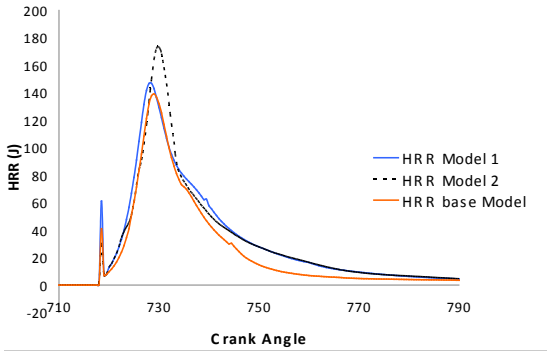

Fig 19. Heat release rates for 3 models.

As seen in Figure 19, the primary maximum of HRR (Heat Release Rate) for model 2 is smaller than the others. Its effects are seen as pressure reduction after SOI in model 2. By increasing velocity, reducing temperature in SOI, and small differences between the turbulent kinetics energy are the reasons of this phenomenon. In diffusion combustion, HRR of model 2 is larger than the base model and is equal to its value in model 1.

HRR in the primary maximum of model 1 (premixed combustion) has higher values than the other two models which is due to temperature raise at SOI and swirl dominant mixing air and fuel.

As shown in Figure 20, the start of combustion in model 2 and base model are similar but the maximum value of the premixed combustion in model 2 is smaller than the base model which approves the pervious results.

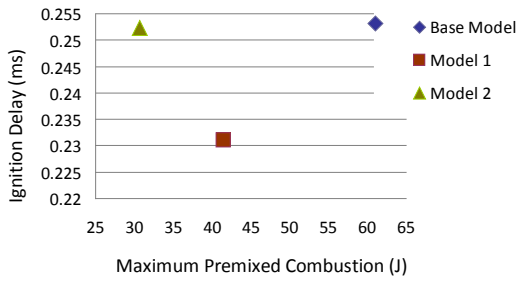

Fig 20. relation between ignition delay and maximum premixed combustion.

According to the literature, increasing swirl ratio of the fluid at SOI leads to an increase in NOx pollutant as a result of enhancement at the local air fuel mixture and raise in local combustion temperature. In other words, increasing premixed combustion raises this pollutant. However, as shown in Figure 19, the maximum value of premixed combustion for model 2 does not follow an increasing trend and even has 30% reduction (which leads to reduction in NOx pollutant). Regarding temperature graphs shown in Figure 21, compared with base model, temperature of the model 2 in SOI has 35 degrees differences. Reason of this phenomenon is discussed in the previous section. Regarding HRR in diffusion combustion and better air fuel mixing due to enhancing swirl, more heat will release from the burnt fuel. This leads to mean temperature increase (expansion stroke). Air temperature in model 1 is also less than the base model. As the combustion continues and HRR value increases, the air temperature in model 1 will increase in comparison with the base model. The pollutant production is directly related to temperature increase trend in the combustion (Figure 21).

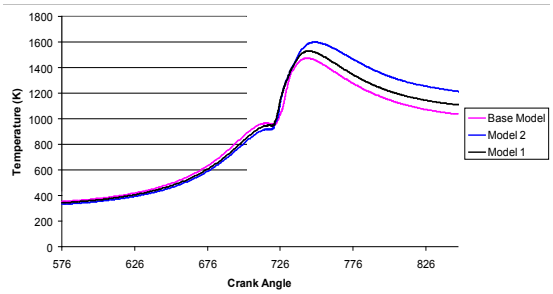

Fig 21. Combustion chamber temperature curve

The NOx formation trend for three models is shown in

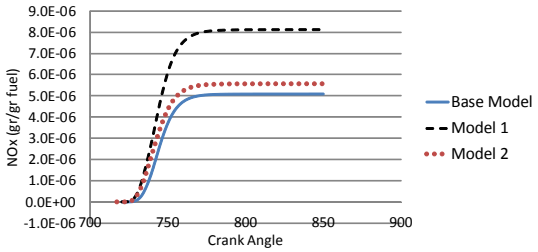

Fig 22. NOx mass fraction in three models.

As shown in Figure 22, due to increasing swirl in model 2 and temperature increase, there is no significant raise in NOx value. The NOx value in model 2 is 18.69% more than the base model, while it is 80.6% in model 1. This is due to small differences in turbulent kinetic energy between model 1 and model 2. Moreover, the relative temperature in model 2 is lower than the other two models. This leads to reducing the maximum HHR value (premixed combustion) which is shown in Figure 23.

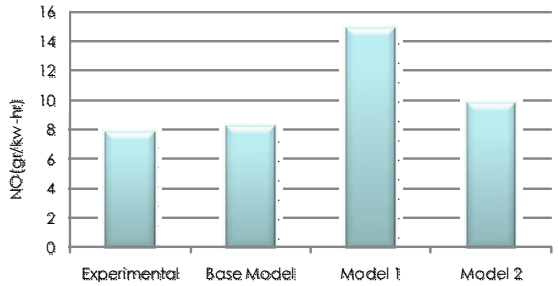

Fig 23. NOx emission of three models.

Opposite to NOx, soot pollutant formation and oxidation has a specific trend. The soot pollutant reduces with increasing swirl ratio and enhancing local mixing of air and fuel accompany with temperature increase.

In other words, oxidation of this pollutant decreases with the increase of the chamber mean temperature. Soot mass fraction in the three models is shown in the Figure 24.

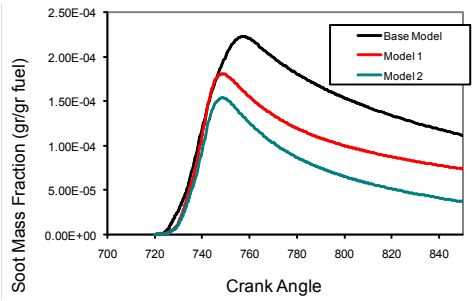

Fig 24. Soot pollutant formation and oxidation in the three models.

As shown in Figure 24, soot formation and oxidation has a specific trend. In an engine, soot value is proportional to HRR and local fuel air mixture. Increasing swirl and local air fuel mixing, model 1 and 2 has lower soot value than the base engine, respectively.

Due to the lower temperature and velocity structure in base chamber, less time is available for soot oxidation, so it has higher soot value as compared to other chambers. This trend is shown using bar graphs in Figure 25.

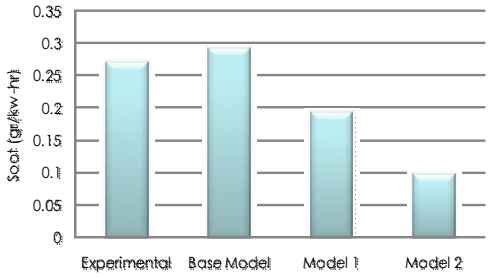

Fig 25. Soot pollutant in 3 models.

Regarding the results achieved from pollutant analysis, soot pollutant in model 1 has decreased by 33.82% relative to the base model. However, this reduction in model 2 is 66.87%. These results can be described using Figure 26.

Cross sectional areas shown in Figure 26 are top view of cylinder, between cylinder head and piston crown. As demonstrated in this Figure NOx pollutant in model 1 has higher value than the other two models. The pollutant formation rate in model 1 is also higher which verifies the curves shown in the Figure 22. Regarding the Figure, more regions in model 1 has higher temperature values. However, as described in the previous sections, NOx formation is more influenced by the early maximum value of HRR. Therefore, NOx value in the second model is less than the first one.

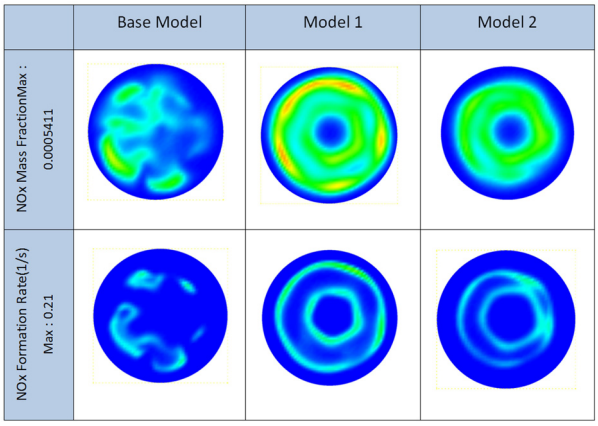

Fig 26. Mass fraction and NOx formation rate at 30 ATDC.

Mass fraction and NOx formation rate at 30 ATDC is shown in Figure 26. Regarding Figure 22 the formation rate of this pollutant has been reduced such that its maximum value has become 0.21 lit/sec. However, after this stage NOx formation rate is dramatically reduced and the polluted value remains constant till EVO (Exhaust Valve Open). Soot pollutant has a different procedure. Except base model unlike other models which has little soot oxidation (around 30 ATDC) due to relatively low temperature and swirl. Combustion process in the other two models begins to oxidize the formed soot and this process continues till EVO. Mass fraction and soot pollutant formation rate at 30 ATDC is shown in Figure 27. Regarding this Figure, soot oxidization in model 2 is more than the other two models. This process leads to soot pollutant reduction at EVO. At this moment the overall soot oxidization rate is very low.

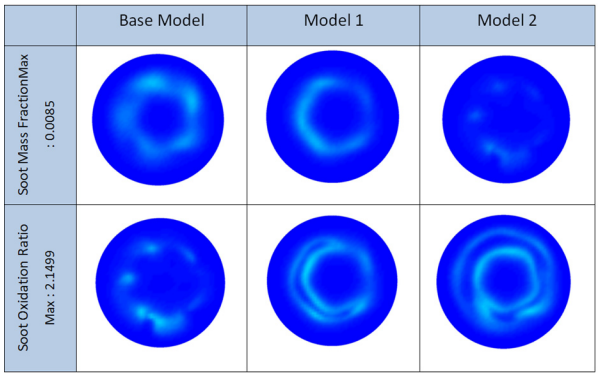

Fig 27. Mass fraction and soot formation rate at 30 ATDC.

Conclusions

In conclusion, by increasing swirl, enhancing diffusion combustion and mixing air and fuel, soot pollutant dramatically reduces in model 2. Obstacles and raise in frictional losses in helical inlet ports causes little reduction in volumetric efficiency which leads to decreasing primary maximum of in-cylinder pressure. The primary maximum of the in-cylinder temperature is also affected by volumetric efficiency.

By enhancing combustion process with enhancing mixing of air and fuel, the indicated power in model 2 is higher than the other two models. In model 2, the flow pattern during induction stroke, swirl increase in compression stroke and consequently increasing heat transfer to the cylinder wall lead to relatively temperature reduction in SOI.

Relative temperature reduction in SOI, slight decrease in volumetric efficiency and minor increase in turbulent kinetic energy lead to reduction in HRR primary maximum. Consequently, it results in little increase in NOx pollutant in model 2 relative to base model.

Enhancing power, reducing BSFC, little increase in NOx pollutant and dramatic reduction in soot pollutant are the main reasons to choose model 2 as the finest model.

Acknowledgement

Special thanks from Dr. Khoshbakhti saray from University of Sahand–Iran for his useful guides.

References:

[1].Yufeng Li Cross. “Effect of Combinations and Orientation of Intake Port On Swirl Motion in four-Valve DI Diesel Engine.” SAE, No. 2002-01-1823.

[2]. J. David Rathnaraj and Prof. T. Michael. N. Kumar. “Studies on Variable Swril Intake System for DI Diesel Engine Using CFD.” International Journal of Applied Engineering Research (2007): 383-393.

[3]. Philip W. Stephenson, Peter J. Claybaker and Christopher J. Rutland. “Modeling the Effects of Intake generated Turbulence and Resolved Flow Structures on Combustion in DI Diesel Engines.” SAE No. 940434.

[4]. C. J. Rutland, C. M. Pieper, and R. Hessel. “Intake and Cylinder Flow Modeling with a Dual-Valve Port.” SAE No. 930069.

[5]. Kang Y. Huh, Chang Ryol Choi, and Jong Gyu Kim. “Flow Analysis of the Helical Intake Port and Cylinder of a Direct Injection Diesel Engine.” SAE No. 952069.

[6]. Jun-ichi Kawashima, Hiroshi Ogawa and Yoshiyuki Tsuru. “Research on a Variable Swirl Intake Port for 4-Valve High-Speed DI Diesel Engines.” SAE No. 982680.

[7]. T. R. Fuchs and C. J. Rutland. “Intake Flow Effects on Combustion and Emissions in a Diesel Engine.” SAE No. 980508.

[8]. Naber, J. D., Reitz, R . D. “Modeling Engine Spray/Wall Impingement.” SAE Paper NO. 880107.

[9]. Zur Loye AO, Siebers DL, McKinley TL, Ng HK, Primus RJ. “Cycle-Resolved LDV Measurements in a Motored Diesel Engine and Comparison with k-e Model Predictions.” SAE No.890618.

[10]. AVL Fire, V8.3. Help. Part: General Species Transport Model Equation, Page 11-15.